# Orthorhombic $ScB_3$ and hexagonal $ScB_6$ with high hardness

Kaixuan Zhao,[1] Qianyi Wang,[1] Wenjing Li,[1] Qiuping Yang,[1] Hong Yu,[1] Fanjunjie Han,[1] Hanyu Liu,[2,*] and Shoutao Zhang[1,†]

[1]*Centre for Advanced Optoelectronic Functional Materials Research and Key Laboratory for UV Light-Emitting Materials and Technology of Ministry of Education, Northeast Normal University, Changchun 130024, China*

[2]*International Center for Computational Method & Software and State Key Laboratory of Superhard Materials, College of Physics, Jilin University, Changchun 130012, China*

(Received 16 November 2021; revised 12 January 2022; accepted 22 February 2022; published 8 March 2022)

Transition metal borides (TMBs) have received great interest since these intriguing borides could be considered potential applications for designing exotic materials with distinguished properties such as superhardness. The search for TMBs regarding high hardness value remains urgent. Given that Sc is the lightest transition metal element that often exhibits unique properties, in this paper, we undertake a comprehensive investigation of the Sc-B system at high pressures using the state-of-the-art structure search method within the framework of first-principles electronic structure. As a result, our structure searches identified several stable Sc-B phases (i.e., ScB, $ScB_3$, $ScB_4$, and $ScB_5$) as well as a metastable $ScB_6$. Strikingly, among these scandium borides, *Pnma* $ScB_3$ contains a boron framework with open channels, while $ScB_6$ possesses interlinking boron trimer units. Remarkably, our simulations suggest the hard features of *Pnma* $ScB_3$ and $P6_3mc$ $ScB_6$ with high simulated Vickers hardness values of 38.3 and 39.8 GPa, respectively, which are mainly attributed to their peculiar strong covalent boron network. The excellent stability and high hardness of $ScB_3$ and $ScB_6$ render them promising candidates for superhard materials. Additionally, an orthorhombic boron allotrope *o*-$B_{12}$ is predicted by removing Sc from *Pnma* $ScB_3$, where this structure exhibits an estimated hardness value of 24.9 GPa and superconducting critical temperature $T_c$ of 2.9 K at 1 atm. In this paper, we advance the existing knowledge of TMBs as well as provide implications for the search for TMBs with unique properties.

DOI: 10.1103/PhysRevB.105.094104

## I. INTRODUCTION

Boron-based materials previously were found to exhibit fantastic structures and intriguing properties such as superhardness and superconductivity, enabling them to become enchanting candidates for practical applications, mainly dominated by the peculiar electron deficiency of boron [1,2]. To date, a plethora of boron allotropes with excellent hardness have been proposed [1,3–5]. For instance, nonmetallic $\alpha$-$B_{12}$ [6] with an icosahedron basic building block shows a high hardness value of 44.8 GPa [3]. A higher hardness value of 58 GPa has been observed in insulating $\gamma$-$B_{28}$ [6], which contains dumbbell-like $B_2$ cations and icosahedral $B_{12}$ anions [7]. Thereafter, $\gamma$-$B_{28}$ has further been identified to have a low hardness value of ∼30 GPa [8]. Metallic $\alpha$-Ga-type boron with the modification of $B_{12}$ icosahedra has a superhard value of 61.6 GPa [3]. On the other hand, boron allotropes with appealing properties can be acquired from predicted metal borides via the removal of metal atoms. Recently, based on precursors *I*4/*mmm* $NaB_4$ and *Pm* $Na_2B_{17}$ with open boron channels, two boron allotropes were denoted as *I*4/*mmm* $B_4$ and *Pm* $B_{17}$, which not only has the estimated superconductivity of 19.8 and 15.4 K but also exhibits calculated hardness values of 27.3 and 26.8 GPa [9]. Very recently, a tetragonal *t*-B with the cage structure produced from predicted *t*-$MnB_{12}$ has been shown to possess the highest critical temperature of 43 K among elemental superconductors at ambient pressure [10]. However, access to boron-based solids with superior mechanical properties just by exploring boron allotropes is limited. Thereby, much effort has been devoted to the investigation of metal borides [2,11].

Transition metal borides (TMBs), a typical class of borides with high valence-electron density and strong covalent bonds, have evoked substantial interest due to their ability to be candidates for superhard materials [12–15]. Until now, numerous hard and superhard TMBs solids with abundant structures and physical properties have been synthesized [16–19] or predicted [20–23]. For instance, synthesized layered $ReB_2$ with puckered boron networks at ambient pressure has ultra-incompressibility with an average hardness value of 48 GPa under a load of 0.49 N [16,24]. Also, $OsB_2$ with an orthorhombic *Pmmn* structure has been experimentally proposed as an ultra-incompressible hard material [25]. Further, $WB_4$ has been measured to show Vickers hardness values from 43.3 to 28.1 GPa at low and high loads, respectively [26]. Recently, the predicted superhard $WB_5$ has been shown to not only possess a Vickers hardness value of 45 GPa and a high fracture toughness value of 4 MPa · $m^{0.5}$ but also to have good stability at ambient pressure and high temperature [27]. Meanwhile, 3*d* transition metal tetraborides with unusual,

*hanyuliu@jlu.edu.cn
†zhangst966@nenu.edu.cn

 

interlinked rhomboid four-membered boron units also elucidate impressive mechanical features [28]. The *Pnnm*-structured $CrB_4$ is estimated to have a high Vickers hardness value of 48 GPa [18]. However, it shows the converged hardness value of 23.3 GPa [29]. Orthorhombic $FeB_4$ with *Pnnm* symmetry was synthesized in a multi-anvil experiment, supporting that the previously predicted orthorhombic structure not only has superconductivity $<2.9$ K but also possesses the high nanoindentation hardness value of 62(5) GPa [30]. Subsequent theoretical studies have further revealed that $FeB_4$ is a hard material with a hardness value of 11.7–32.3 GPa [31]. Regarding rare-earth borides, two high-pressure superconductive phases with *Cmmm* and *I*4/*mmm* symmetry were recently found in $YB_6$ stoichiometry, in which *I*4/*mmm* $YB_6$ has a $B_{24}$ unit [32]. Afterward, a hexagonal *R*-3*m* phase of $YB_6$ was predicted to be more stable than the synthesized cubic *Pm*-3*m* $YB_6$ at ambient pressure and to have a calculated Vickers hardness value of 37.0 GPa [33]. In addition to these intriguing mechanical properties, superconductivity is also observed in TMBs. For example, recent theoretical work has proposed a trigonal $LaB_8$ with boron clathrate structure containing a $B_{26}$ cage, which has superconducting critical temperatures of $\sim$20 K at ambient pressure and 5 K at 70 GPa [34]. Meanwhile, $LaB_8$, containing the clathrate boride with a $B_{26}$ cage, has also been predicted and successfully synthesized at high pressure and temperature, exhibiting the estimated superconductivity of 14 K at 1 atm [35]. Moreover, more boron-rich $ZrB_{12}$ composed of a $ZrB_{24}$ polyhedron has the measured Vickers hardness of 40 GPa under the load of 0.49 N [36]. In view of the above descriptions, TMBs play a vital role in designing superhard materials.

Scandium (Sc), as a first member of transition-metal elements, not only possesses the lightest mass but also has rich valence electrons favoring the formation of diverse scandium borides. A series of Sc-B compounds have been synthesized, including $ScB_2$ [37], $ScB_{12}$ [38], $ScB_{15}$ [39], and $ScB_{19}$ [40]. Particularly $ScB_2$ with *P*6/*mmm* symmetry has hardness values of 41.4–42.1 GPa [41,42]. More B-rich *Fm*-3*m*-structured $ScB_{12}$ has been found to exhibit superhard characteristics with the hardness value of 41.7 GPa [43,44]. Presently, theory prediction plays an important role in hunting scandium borides. A monoclinic compressed *C*2/*m* phase of $ScB_2$ has been found to be transformed from ambient-pressure *P*6/*mmm* $ScB_2$ [45]. Recently, the predicted high-pressure phase *C*2/*m* $ScB_3$ has been found to have outstanding mechanical properties with hardness of 37.1 GPa [42]. More recently, $ScB_4$ has been discovered to undergo a pressure-induced phase transition from orthorhombic *Cmcm* to *Pnma* phase, having calculated hardness values of 34.5 and 31 GPa, respectively [46]. However, detailed information, such as the high-pressure phase diagram and structures with superior properties of the Sc-B system, remains unknown thus far. Simultaneously, most TMBs encompass heavier transition metal elements than scandium. These factors further encourage us to search for emerging scandium borides as good candidates for light transition borides superhard materials.

In this paper, we present a comprehensive study of Sc-B binary compounds with versatile $Sc_xB_y$ ($x = 1$, $y = 1$–6, 12; $x = 2$, $y = 1$, 3; and $x = 3$, $y = 2$) compositions through first-principles structure search. Interestingly, we identify several stable phases (i.e., ScB, $ScB_3$, $ScB_4$, and $ScB_5$) as well as a metastable $ScB_6$ phase. Especially as boron content increases, unique boron arrangements are predicted. Importantly, calculations show that *Pnma* $ScB_3$ and *P*6$_3$*mc* $ScB_6$ exhibit dynamic and thermal stabilities at ambient pressure. More importantly, further study reveals the Vickers hardness values of 38.3 and 39.8 GPa for *Pnma* $ScB_3$ and *P*6$_3$*mc* $ScB_6$, respectively, implying that both are potential superhard materials. Moreover, the stress-strain analysis of *Pnma* $ScB_3$ and *P*6$_3$*mc* $ScB_6$ reveal the crucial role of the rugged boron framework in determining their mechanical properties.

## II. COMPUTATIONAL DETAILS

Based on the stoichiometric ratios of given elements Sc and B and considered pressures, we implement the extensive search of crystal structures of the Sc-B system by exploiting the CALYPSO package [47,48], whose effectiveness has been demonstrated in finding stable or metastable states of investigated systems [49–57]. Structural optimization and calculations of electronic properties are carried out in the framework of density functional theory (DFT) [58,59] as implemented in the Vienna *Ab initio* Simulation Package code [60]. The electron exchange-correlation effects are depicted by the generalized gradient approximation [61] with Perdew-Burke-Ernzerhof [62] functional. The projector augmented-wave [63] pseudopotentials with $3s^2 3p^6 3d^1 4s^2$ (Sc) and $2s^2 2p^1$ (B) treated as valence electrons are exploited to describe the electron-ion interaction. The availability of the selected pseudopotentials is examined by adopting the full-potential linearized augmented plane-wave method as implemented in the WIEN2K code [64] with the equation of states of *P*6/*mmm*-structured $ScB_2$ (Fig. S1 in the Supplemental Material [65]). Energy convergence can be further confirmed by using a cutoff energy of 800 eV and choosing a *k*-point grid [66] with a reciprocal space resolution of $2\pi \times 0.03$ Å$^{-1}$. Phonon dispersion calculations are performed in the PHONOPY code [67] with the supercell method [68]. The *ab initio* molecular dynamics (AIMD) simulations with NVT (N is the number of particles, V is volume, and T is temperature) ensemble using the Nosé-Hoover method [69] is used to evaluate the thermal stability of studied Sc-B phases at different temperatures. The Voigt-Reuss-Hill approximation [70] is used to estimate the bulk modulus, shear modulus, and Young's modulus. The elastic constants are calculated via the stress-strain approach [71]. More details for computational information can be found in the Supplemental Material [65].

## III. RESULTS AND DISCUSSION

### A. Phase stability of Sc-B compounds

To search for high-pressure structures in the Sc-B system, we conduct a broad range of structural searches with simulation cell size up to 4 f.u. for $Sc_xB_y$ ($x = 1$, $y = 1$–6, 12; $x = 2$, $y = 1$, 3; $x = 3$, $y = 2$) stoichiometries at selected pressures of 1 atm, 50, 100, 200, and 300 GPa, and a temperature of 0 K. Subsequently, the structure with the lowest energy for each $Sc_xB_y$ composition is chosen to calculate its formation energy relative to the elemental solids Sc [72–74] and B [6]. The

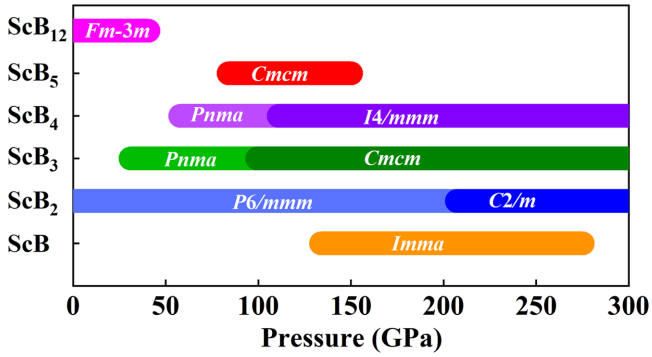


FIG. 1. Pressure stability regions of stable Sc-B phases over a pressure range from 1 atm to 300 GPa. Different colored horizontal bars represent thermodynamic stability pressure ranges of multiple Sc-B phases.

convex hull diagram at different pressures is further constructed through the resulting formation energies (Fig. S2 in the Supplemental Material [65]). The compounds sitting on the solid line are viewed as the thermodynamically stable phases, while compounds located on dotted lines are thermodynamically unstable and decompose into other energetically stable chemical components [75]. Moreover, the previously reported Sc-B phases including *R*-3*m* ScB [42], *P*6/*mmm* $ScB_2$ [37], *C*2/*m* $ScB_3$ [42], *Pnma* $ScB_4$ [46], *Cmcm* $ScB_4$ [46], and *Fm*-3*m* $ScB_{12}$ [38] are adopted to calculate their formation energies with respect to reference phases at ambient pressure. As shown in Table S2 in the Supplemental Material [65], both *P*6/*mmm* $ScB_2$ and *Fm*-3*m* $ScB_{12}$ show negative formation energies at ambient pressure, which indicate that previously synthesized structures are thermodynamically stable. In contrast, *R*-3*m* ScB, *C*2/*m* $ScB_3$, *Pnma* $ScB_4$, and *Cmcm* $ScB_4$ have positive formation energies, suggesting that these structures are thermodynamically unstable. These results are in good agreement with the convex hull diagram of the Sc-B system at 1 atm (Fig. S2 in the Supplemental Material [65]). To accurately determine the pressure range of each stable Sc-B phase, we further establish the pressure-composition phase diagram. As shown in Fig. 1, *Imma* ScB is predicted to become stable in the pressure range of 133.8–275.1 GPa. For B-rich $ScB_2$, the low-pressure *P*6/*mmm* [37] and high-pressure *C*2/*m* [45] phases are well reproduced, indicating the reliability of our structure search. Moreover, the transition pressure of 207.2 GPa is in good agreement with the previously reported results [45]. The *Pnma* $ScB_3$ is stable from 31.0 GPa and converts to the *Cmcm* phase at a higher pressure of 99.3 GPa. As the B content increases, previously proposed *Pnma* $ScB_4$ is found to be transformed into *I*4/*mmm* $ScB_4$ [46] >111.0 GPa. For more B-rich $ScB_5$, *Cmcm* $ScB_5$ is stable from 83.9 to 150.1 GPa. For the most B-rich $ScB_{12}$, the previously known *Fm*-3*m* phase [38] is also identified and has a stability pressure range from 1 atm up to 40.6 GPa. Notably, further simulations illustrate that $P6_3mc$-structured $ScB_6$ has formation enthalpy of 11 meV/atom above the convex hull relative to neighboring reference phases *Pnma* $ScB_3$ and $\gamma$-$B_{28}$ [6] at 50 GPa (Table S3 in the Supplemental Material [65]). It is found that the synthesized metastable materials account for 20% of the synthesized materials in the organic crystal structure database. Some of these metastable materials have formation energies of ∼50 meV/atom [76,77]. The above analysis demonstrates that $P6_3mc$ $ScB_6$ is metastable. Its stability will be discussed in detail later. Furthermore, to examine the dynamic stabilities of predicted Sc-B phases, we calculated their phonon spectra. It is noted that there is no imaginary phonon frequency in predicted structures, indicating that they are dynamically stable (Fig. S3 in the Supplemental Material [65]).

### B. Geometric configurations

Among these identified Sc-B phases, ScB has an orthorhombic structure [space group *Imma*, 4 f.u. per cell, Fig. 2(a)]. This structure can be viewed as the face-sharing stacking of the $ScB_9$ dodecahedron. Each Sc atom is surrounded by nine B atoms with Sc-B distance of 2.18–2.58 Å at 200 GPa. Here, B atoms exhibit one-dimensional zigzaglike chains with a B-B bond length of 1.53 Å, which further constitute a sandwich structure with Sc atoms along the *c* axis [Fig. 2(b)].

For B-rich $ScB_3$, its low-pressure phase crystallized into an orthorhombic structure in *Pnma* symmetry [4 f.u. per cell, Fig. 2(c)], which consists of the $ScB_{13}$ polyhedron with Sc-B distances of 2.27–2.50 Å at 50 GPa. Three types of B sites are found in this structure, namely, B1, B2, and B3. Interestingly, *Pnma* $ScB_3$ not only contains a boron triangle consisting of B1, B2, and B3 atoms with distance of 1.67–1.84 Å but also has a quadrilateral boron unit comprising B1 and B2 atoms with bond length of 1.82–1.84 Å. These edge-sharing three- and four-membered boron units are linked by B1-B3 bonds with distance of 1.73 Å and further form a boron framework with open channels along the *b*-axis direction, where Sc atoms are staggered. Upon further compression, $ScB_3$ undergoes a phase transition to another orthorhombic *Cmcm* structure [4 f.u. per cell, Fig. 2(e)]. Evidently, the face-sharing $ScB_{15}$ decahedron as the basic building block of this structure comprises one Sc and its neighboring 15 B atoms with Sc-B distance of 2.06–2.50 Å at 300 GPa. Meanwhile, there are three inequivalent B positions (i.e., B1, B2, and B3). Interestingly, B1 and B2 atoms form a two-dimensional buckled layer with two kinds of B1-B2 bond lengths of 1.59 and 1.61 Å at 300 GPa, whereas B3 atoms have a serrationlike chain structure with slightly short B3-B3 bond length of 1.53 Å. These two kinds of boron arrangements are linked by B1-B3 bonds with equal distance of 1.56 Å and further constitute the whole B skeleton.

For B-rich $ScB_4$, the predicted high-pressure phase adopts a tetragonal structure with *I*4/*mmm* symmetry [2 f.u. per cell, Fig. 2(g)], which is isostructural to those of *I*4/*mmm*-structured $LiB_4$ [78] and $NaB_4$ [9]. This structure is composed of a face-sharing $ScB_{18}$ dodecahedron with Sc-B distance of 2.05–2.52 Å at 300 GPa. Interestingly, these B atoms form an open framework with B-B bond lengths of 1.58 and 1.89 Å, while the Sc atom is located at the center of the boron framework [Fig. 2(h)].

With further increase in B content, $ScB_5$ adopts an orthorhombic structure with space group *Cmcm* [4 f.u. per cell, Fig. 2(i)], where each Sc atom is surrounded by 17 neighboring B atoms with Sc-B distance of 2.18–2.43 Å at 100 GPa. This structure consists of $ScB_{17}$ octahedron via the

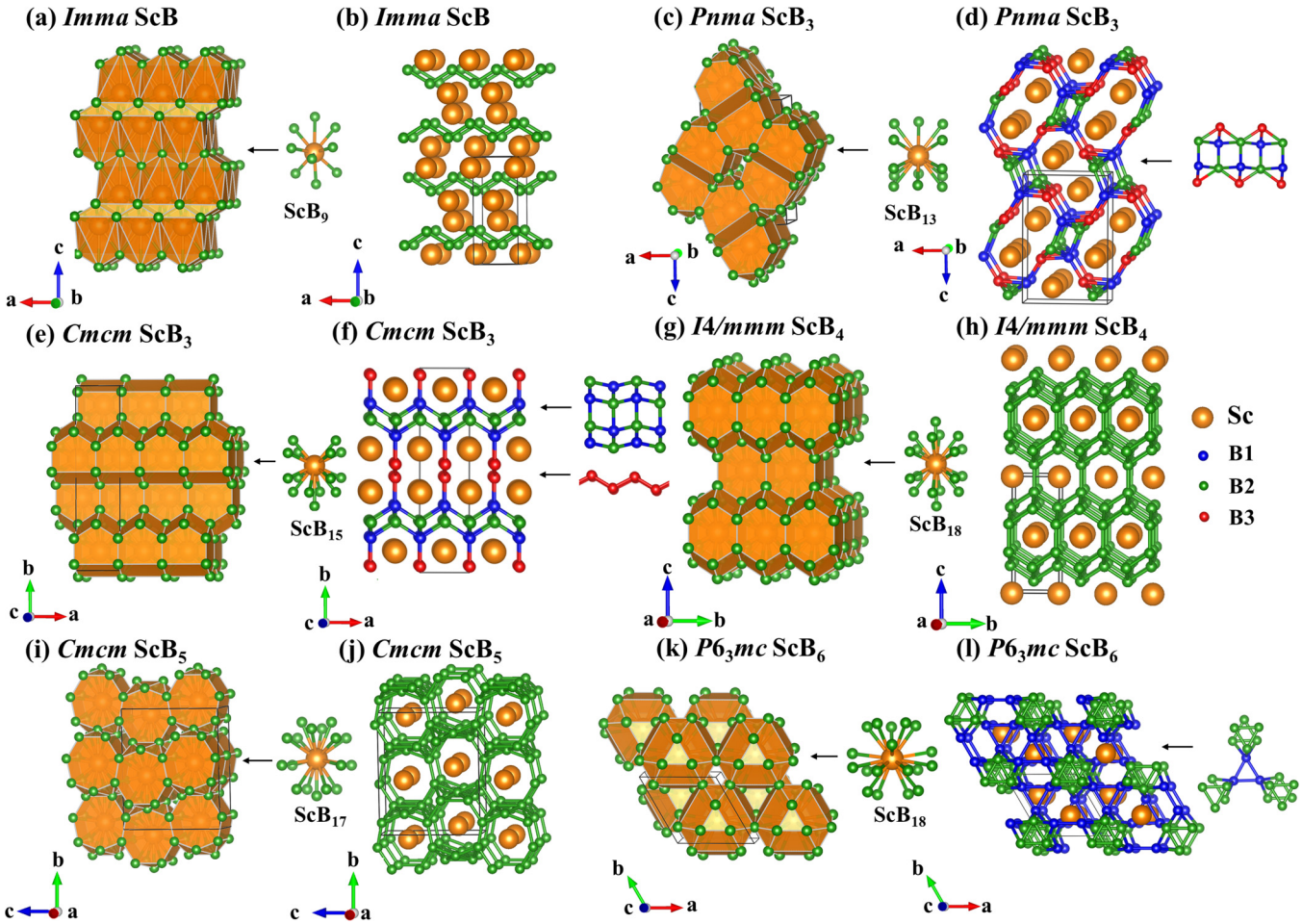


FIG. 2. Crystal structures of predicted Sc-B phases. (a) *Imma* ScB with $ScB_9$ polyhedron at 200 GPa. (b) Zigzag B chain in *Imma* ScB. (c) Polyhedron view of *Pnma* $ScB_3$ at 50 GPa. (d) *Pnma* $ScB_3$ with face-sharing B units. (e) *Cmcm* $ScB_3$ containing $ScB_{15}$ unit at 300 GPa. (f) *Cmcm* $ScB_3$ with boron layer and boron chain. (g) *I*4/*mmm* $ScB_4$ at 300 GPa with $ScB_{18}$ polyhedron. (h) Open B framework in *I*4/*mmm* $ScB_4$. (i) The coordination number of Sc atoms is 17 in *Cmcm* $ScB_5$ at 100 GPa. (j) Cage-type B structure in *Cmcm* $ScB_5$. (k) Metastable $P6_3mc$ $ScB_6$ with $ScB_{18}$-polyhedral unit at 50 GPa. (l) Interconnecting triangular $B_3$ motif in $P6_3mc$ $ScB_6$.

face-sharing packing arrangements. It is worth noting that the three-dimensional clathratelike B frame with bond lengths of 1.58–1.80 Å.

For stoichiometry $ScB_6$ with high B concentration, its metastable phase exhibits a hexagonal structure [space group $P6_3mc$, 2 f.u. per cell, Fig. 2(k)]. It should be noted that each Sc atom has 18 coordinations with Sc-B distances of 2.29–2.51 Å at 50 GPa. There are two distinct B positions in the conventional cell of $P6_3mc$ $ScB_6$, namely, B1 occupying Wyckoff site 6*c* (0.4078, 0.2039, 0.1156) and B2 locating at Wyckoff site 6*c*. Strikingly, both B1 and B2 (0.8796, 0.7592, 0.4116) atoms form B triangle units with equal B1-B1 distance of 1.65 Å and the same B2-B2 distance 1.77 Å at 50 GPa, respectively. Further, these B trigons interconnected through B1-B2 bonds with bond lengths of 1.68 and 1.76 Å are assembled into the boron network, in which each B2 atom is coordinated by adjoining threefold B1 atoms [Fig. 2(l)].

### C. Dynamic and thermal stabilities

To validate whether these predicted Sc-B phases can be recoverable to ambient pressure, their phonon calculations at 1 atm are performed. Strikingly, only *Pnma* $ScB_3$ and $P6_3mc$ $ScB_6$ are dynamically stable with the absence of imaginary phonon modes in their respective Brillouin zone [Figs. 3(a) and 3(b)]. The phonon density of states (PHDOS) of *Pnma* $ScB_3$ show the phonon dispersion curves can be divided into two regions: high-frequency modes >25.3 THz mainly arise from the vibrations of B atoms, whereas low-frequency ones <21.3 THz come from the coupled vibrations of Sc and B atoms [Fig. 3(c)]. Comparatively, the phonon dispersion curves of $P6_3mc$ $ScB_6$ contain five separate groups, including low-frequency acoustic branches <7.8 THz mainly provided by the coupled vibrations between Sc and B atoms, medium-frequency optic ones (10.3–21.6, 22.7–24.5, and 25.7–26.4 THz) originating from the vibrations of B atoms, and high-frequency optic ones >29.9 THz dominated by B atom vibrations [Fig. 3(d)]. Subsequently, we conduct AIMD simulations to examine the thermal stabilities of *Pnma* $ScB_3$ and $P6_3mc$ $ScB_6$ at the temperature range of 300–1000 K with the time step of 1 fs and supercells of 96 and 112 atoms for $ScB_3$ and $ScB_6$, respectively. The simulated results demonstrate that *Pnma* $ScB_3$ and $P6_3mc$ $ScB_6$ remain stable at 300 K (Fig. S4 in the Supplemental Material [65]) and

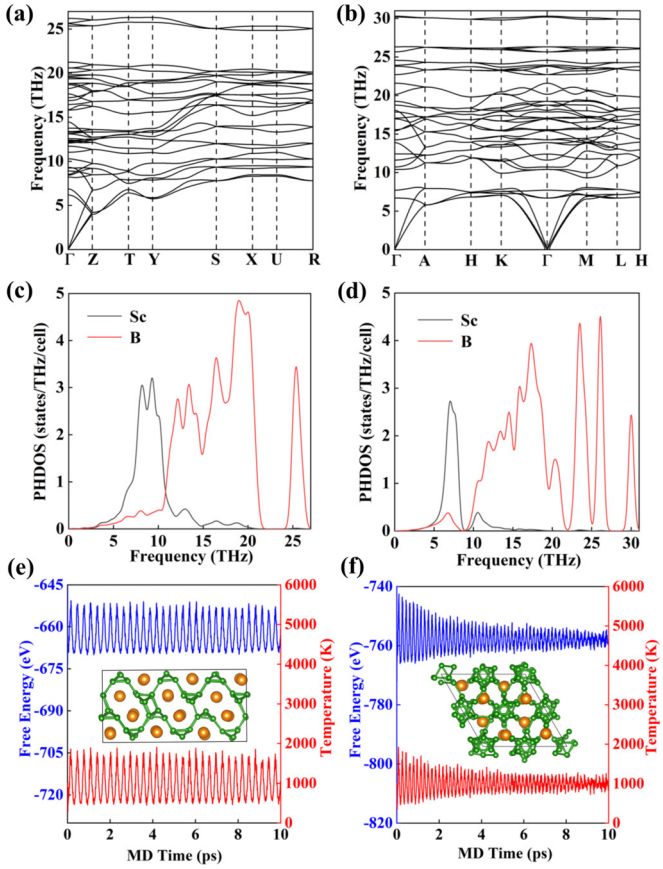


FIG. 3. Calculated phonon dispersion curves of (a) *Pnma* $ScB_3$ and (b) $P6_3mc$ $ScB_6$ at 1 atm. Phonon density of states (PHDOS) of (c) *Pnma* $ScB_3$ and (d) $P6_3mc$ $ScB_6$ at 1 atm. The free energy fluctuations of (e) *Pnma* $ScB_3$ and (f) $P6_3mc$ $ScB_6$ vary with the time step of the molecular dynamics simulation at 1000 K. The inset indicates the resultant snapshot of the simulated system after 10 ps.

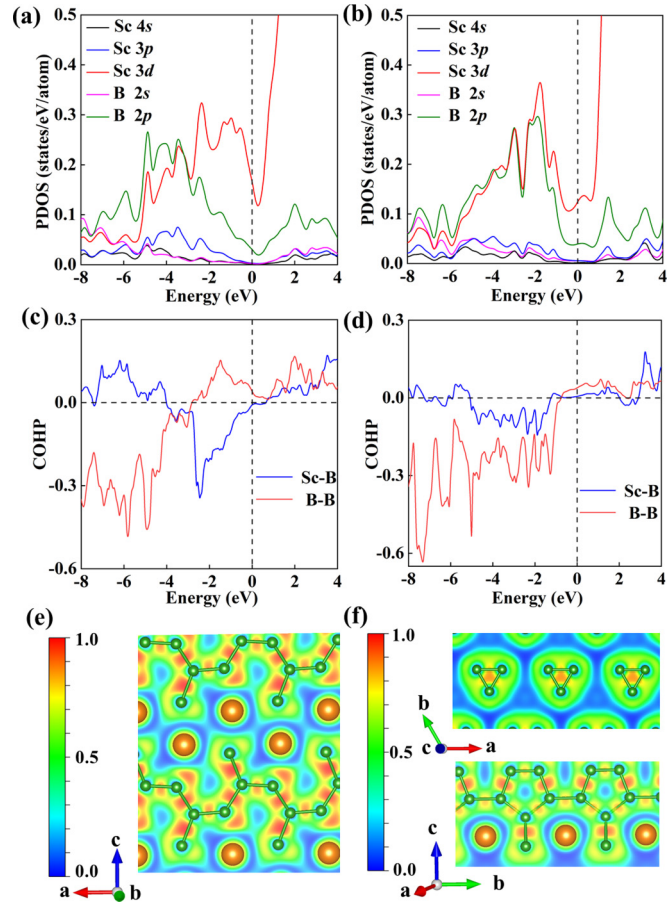


FIG. 4. Projected density of states (PDOS) of Sc and B atoms in (a) *Pnma* $ScB_3$ and (b) $P6_3mc$ $ScB_6$ at 1 atm. The vertical dashed line denotes the Fermi energy. Crystal orbital Hamiltonian population (COHP) of (c) *Pnma* $ScB_3$ and (d) $P6_3mc$ $ScB_6$. The horizontal dashed line represents the Fermi level. Electron localization function (ELF) of (e) *Pnma* $ScB_3$ and (f) $P6_3mc$ $ScB_6$ at 1 atm.

even higher temperature of 1000 K [Figs. 3(c) and 3(d)]. Furthermore, the terminal structures at 10 ps of *Pnma* $ScB_3$ and $P6_3mc$ $ScB_6$ in the insets imply that they keep the structure integrity (Fig. S4 in the Supplemental Material [65]). Moreover, the calculated elastic constants for orthorhombic *Pnma* $ScB_3$ and hexagonal $P6_3mc$ $ScB_6$ demonstrate that they meet the mechanical stability based on Born stability criteria [79] (Table S4 in the Supplemental Material [65]). In view of the above analysis, *Pnma* $ScB_3$ and $P6_3mc$ $ScB_6$, once synthesized under pressure, are likely to be accessible to ambient conditions. In addition, the removal of metal atoms from metal-containing compounds has become a viable way for obtaining elemental allotropes [9,10,80,81]. Surprisingly, an orthorhombic B allotrope *Pnma* $B_{12}$ named *o*-$B_{12}$ is gained via removing Sc atoms from *Pnma*-structured $ScB_3$ and retains B arrangements analogous to that of *Pnma* $ScB_3$ (Fig. S5(a) in the Supplemental Material [65]). Its dynamical stability at ambient pressure is further checked (Fig. S5(b) in the Supplemental Material [65]). Meanwhile, *o*-$B_{12}$ exhibits good thermal stability at temperatures of 300 and 1000 K (Figs. S6(a) and S6(b) in the Supplemental Material [65]).

### D. Electronic properties and chemical bonding

The intriguing structures of *Pnma* $ScB_3$ and $P6_3mc$ $ScB_6$ further inspire us to investigate their electronic properties. The computed electronic band structures and projected density of states (PDOS) simulations suggested the metallic features of *Pnma* $ScB_3$ and $P6_3mc$ $ScB_6$ at 50 GPa (Fig. S7 in the Supplemental Material [65]). Interestingly, when decompressed to ambient pressure, *Pnma* $ScB_3$ and $P6_3mc$ $ScB_6$ maintain metal characteristics [Figs. 4(a) and 4(b)]. The PDOS analysis of $ScB_3$ and $ScB_6$ show that the Sc 3*d* orbital near the Fermi level plays a dominant role in their metallicity. Meanwhile, there is pronounced overlap between Sc 3*d* and B 2*p* below the Fermi level, implying the strong interaction between Sc and B atoms. In addition, other predicted compressed Sc-B compounds are also metallic phases (Fig. S7 in the Supplemental Material [65]).

To understand interatomic interactions, we further calculate the crystal orbital Hamilton populations (COHPs) as implemented in the LOBSTER code [82,83] of adjacent Sc-B and B-B pairs in *Pnma* $ScB_3$ and $P6_3mc$ $ScB_6$ at 1 atm. In general, the negative and positive COHPs represent the bonding and antibonding states, respectively. As illustrated in Fig 4(c),

the COHP of B-B has apparent negative ones below the Fermi energy for *Pnma* $ScB_3$, suggesting that B-B interactions dominate structural stability. Further decomposed COHPs indicate that the B-atom interactions predominantly originate from the overlap of B $2p$ orbitals, whereas the orbital overlap of Sc $3d$ and B $2p$ dominate the ones between Sc and B atoms (Fig. S8 in the Supplemental Material [65]). Additionally, the integral COHPs (ICOHPs) up to the Fermi level can measure the bond strength. The resultant ICOHPs of Sc-B and B-B pairs are $-1.965$ and $-2.969$ eV/pair, respectively, demonstrating that B-B interactions are distinctly stronger than that of Sc-B (Table S6 in the Supplemental Material [65]). Similar results are also observed in $P6_3mc$ $ScB_6$ [Fig. 4(d)].

To further unveil the chemical bonding feature of *Pnma* $ScB_3$ and $P6_3mc$ $ScB_6$, their electron localization functions (ELFs) at 1 atm are calculated. As illustrated in [Figs. 4(e) and 4(f)], evident electron localization exists between boron atoms, indicating the formation of strong B-B bonds with covalency. In comparison, ionic bonds are formed between Sc and B atoms, which is in accordance with the above PDOS analysis and supported by further Bader charge analysis (Table S7 in the Supplemental Material [65]). Overall, the structural stabilities of $ScB_3$ and $ScB_6$ are mainly attributed to the contribution of Sc-B ionic bonds and strong B-B bonding. In addition, the ionic Sc-B and covalent B-B bondings are also found in other predicted Sc-B phases (Fig. S9 in the Supplemental Material [65]).

Meanwhile, electron structure analyses show that $o$-$B_{12}$ exhibits a metallic character at ambient pressure (Fig. S10 in the Supplemental Material [65]). Stimulated by the metallicity of $o$-$B_{12}$, we explore its superconductivity at 1 atm through the Allen-Dynes modified McMillan equation [84,85], adopting a representative Coulomb pseudopotential $\mu^*$ of 0.1 within the framework of the Bardeen-Cooper-Schrieffer [86] theory. The electron-phonon coupling study reveals that $o$-$B_{12}$ is a superconductor with a critical temperature $T_c$ of 2.9 K at ambient pressure (Table S8 in the Supplemental Material [65]).

### E. Mechanical properties

The robust dynamical, thermal, and mechanical stabilities at atmospheric pressure and strong covalent boron frames of $ScB_3$ and $ScB_6$ motivate us to investigate their mechanical properties at ambient pressure. Using the empirical model $H_v = 2.0(k^2G)^{0.585}$–$3.0$ ($k = G/B$, $G$ is shear modulus, $B$ is bulk modulus) [87], the Vickers hardness values of *Pnma* $ScB_3$ and $P6_3mc$ $ScB_6$ are calculated to be 38.3 and 39.8 GPa, respectively (Table S4 in the Supplemental Material [65]), which are marginally higher than 37.0 GPa of recently reported $YB_6$ [33] and comparable with that of $ZrB_{12}$ [36] (40 GPa) and $WB_4$ [26] (43 GPa) under the load of 0.49 N. Most interestingly, the rigidity values of *Pnma* $ScB_3$ and $P6_3mc$ $ScB_6$ are comparable with 40 GPa of the standard criterion of superhard materials [88–91]. Furthermore, the fracture toughness is estimated by the following empirical model: $K_{IC} = \alpha V^{1/6} G(B/G)^{1/2}$ [92], where $\alpha$ denotes the enhancement factor accounting for the degree of metallicity, and $V$ is the volume per atom in units of cubic meters. For insulators, semiconductors, carbides, nitrides, and borides, $\alpha = 1$. The calculated results show that *Pnma* $ScB_3$ and $P6_3mc$ $ScB_6$ have fracture toughness values of 2.97 and 2.95 MPa $m^{0.5}$, respectively (Table S4 in the Supplemental Material [65]), both of which are comparable with TiC [92] (3.10 MPa $m^{0.5}$), SiC [92] (3.11 MPa $m^{0.5}$), and $B_4C$ [92] (2.91 MPa $m^{0.5}$). Moreover, the calculated densities of *Pnma* $ScB_3$ (3.70 g/$cm^3$) and $P6_3mc$ $ScB_6$ (3.26 g/$cm^3$) are comparable with or lower than that of diamond (3.52 g/$cm^3$), respectively (Table S4 in the Supplemental Material [65]). These results indicate that they are promising lightweight incompressible superhard materials. Furthermore, we recalculate the Vickers hardness of previously proposed Sc-B compounds including $R$-$3m$ ScB [42], $P6/mmm$ $ScB_2$ [37], $C2/m$ $ScB_3$ [42], *Pnma* $ScB_4$ [46], $Cmcm$ $ScB_4$ [46], and $Fm$-$3m$ $ScB_{12}$ [38] and find that $P6/mmm$ $ScB_2$, $C2/m$ $ScB_3$, $Cmcm$ $ScB_4$, and $Fm$-$3m$ $ScB_{12}$ exhibit high hardness values comparable with 40 GPa, suggesting that they are also potential candidates for superhard materials (Table S5 in the Supplemental Material [65]). Overall, $ScB_2$, $ScB_3$, $ScB_4$, $ScB_6$, and $ScB_{12}$ compounds can be considered candidates for experimental synthesis. Interestingly, $o$-$B_{12}$ has an estimated Vickers hardness of 24.9 GPa (Table S4 in the Supplemental Material [65]), which is higher than $c$-$B_{24}$ [4] (23.1 GPa) and slightly lower than $I4/mmm$ $B_4$ [9] (27.3 GPa) and $Pm$ $B_{17}$ [9] (26.8 GPa). Additionally, it has a calculated fracture toughness of 2.37 MPa $m^{0.5}$ (Table S4 in the Supplemental Material [65]). These indicate that $o$-$B_{12}$ is also an underlying hard elemental material and further demonstrate that the three-dimensional boron framework plays a critical role in the mechanical properties of *Pnma* $ScB_3$.

Based on the high hardness of *Pnma* $ScB_3$ and $P6_3mc$ $ScB_6$, we further perform the in-depth study of their mechanical properties through the stress-strain relationships, which can accurately depict the ideal tensile/shear strengths, structural deformation, and breaking mechanisms of materials under various loading strain conditions [93–103]. Here, we firstly carry out the calculations of tensile strength of *Pnma* $ScB_3$ along a selected series of high-symmetry crystallographic directions to investigate the resistance ability to the tension. The strong tensile stress responses in [100], [010], [001], [110], [011], and [111] are revealed to have peak stresses at 48.0, 35.0, 24.3, 28.5, 28.4, and 25.4 GPa, respectively, which indicate that the ideal tensile strength of *Pnma* $ScB_3$ is 24.3 GPa [Fig. 5(a)]. The corresponding [001] is the weakest tensile direction, making (001) the easy cleavage plane. It is noted that the tensile stress at the strain of 0.08 in the [001] direction drops sharply relative to the peak value, which is dominantly attributed to the breaking of B1-B2, B3-B4, B5-B6, and B7-B8 bonds acting as the main load-bearing components [Fig. 5(f)]. It can be also clearly elucidated that these equal boron-boron distances of 3.26 Å at a tensile strain of 0.08 are obviously >1.92 Å in the structure at equilibrium [Fig. 5(e)]. Further stress-strain relations of *Pnma* $ScB_3$ under shear strains in the (001) plane along [110], [100], and [010] shear slip directions are examined [Fig. 5(b)]. Interestingly, $ScB_3$ exhibits an almost isotropic stress response in a small shear deformation range. With further increase in strain, different shear stress peak values occur in the (001)[110] (24.5 GPa at a strain of 0.14), (001)[100] (20.9 GPa at a strain of 0.12), and (001)[010] (27.4 GPa at a strain of 0.16) directions, exhibiting obvious anisotropic stress

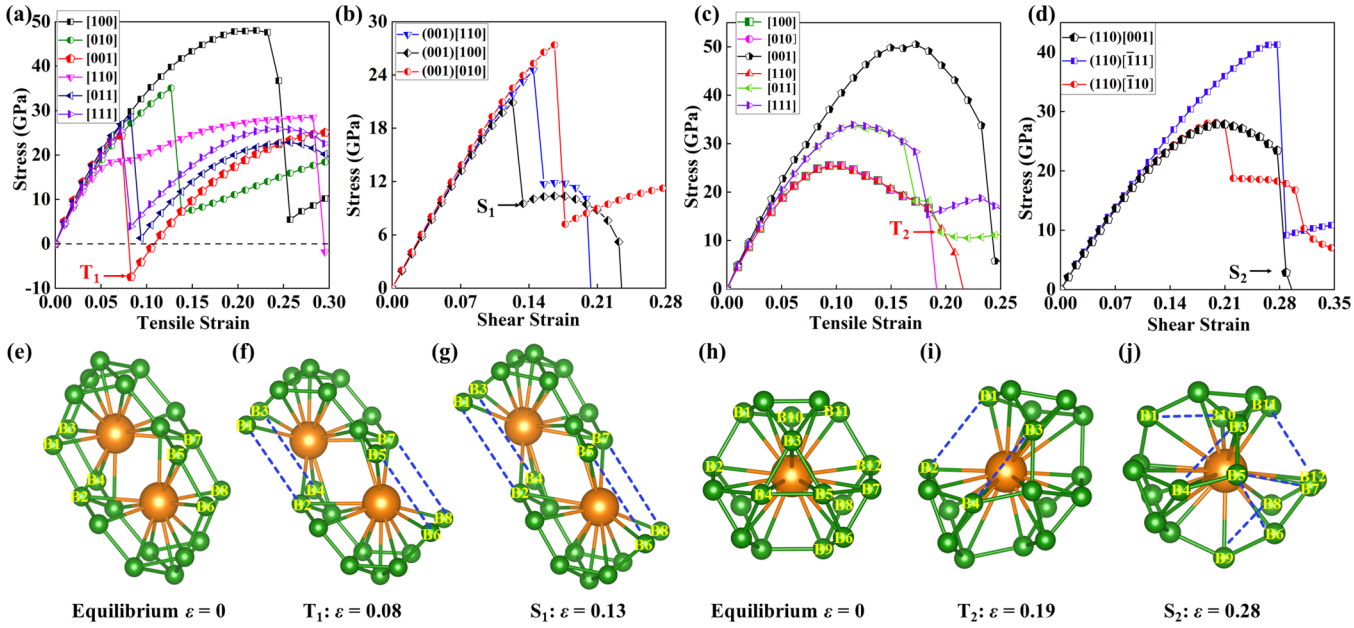


FIG. 5. Stress-strain relations of *Pnma* $ScB_3$ under different (a) tensile and (b) shear deformations. Stress-strain relations of $P6_3mc$ $ScB_6$ under different (c) tensile and (d) shear deformations. (e) Structure of *Pnma* $ScB_3$ at $\varepsilon = 0$. (f) Structure of *Pnma* $ScB_3$ at $\varepsilon = 0.08$ under tensile stress. (g) Structure of *Pnma* $ScB_3$ at $\varepsilon = 0.13$ under shear stress. (h) Structure of $P6_3mc$ $ScB_6$ at $\varepsilon = 0$. (i) Structure of $P6_3mc$ $ScB_6$ at $\varepsilon = 0.19$ under tensile stress. (j) Structure of $P6_3mc$ $ScB_6$ at $\varepsilon = 0.28$ under shear stress.

response [Fig. 5(b)]. The lowest shear stress with a peak value of 20.9 GPa is found in the (001)[100] direction, accompanied by a sudden drop past the peak to 9.5 GPa at a strain of 0.13. To better understand the underlying mechanism, the strain-dependent bond lengths are calculated (Fig. S11(b) in the Supplemental Material [65]). It can be illustrated that the B1-B2, B3-B4, B5-B6, and B7-B8 bond lengths are apparently elongated from 1.92 Å ($\varepsilon = 0$) to 2.12 Å ($\varepsilon = 0.12$). As shear strain increases to 0.13, corresponding B1-B2, B3-B4, B5-B6, and B7-B8 distances show a dramatic increase from 1.92 to 3.60 Å, implying the breaking of these bonds and thus leading to the significant reduction in shear stress [Fig. 5(g)].

By contrast, regarding $P6_3mc$ $ScB_6$, the stress peak values are 25.5, 25.5, 50.5, 25.3, 33.7, and 33.9 GPa under the [100], [010], [001], [110], [011], and [111] tensile deformations [Fig. 5(c)], which suggest that the ideal tensile strength of $P6_3mc$ $ScB_6$ corresponds to the [110] deformation with the lowest peak value of 25.3 GPa, illustrating that the (110) plane is the easy cleavage plane. The lowest tensile stress is slightly >24.3 GPa of *Pnma* $ScB_3$ and comparable with 28.4 GPa of ZrN [104]. Interestingly, the [110] tensile stress gradually reduces after the peak at $\varepsilon = 0.11$ and the extended tensile strain range is observed, which is in stark contrast with *Pnma* $ScB_3$. This unusual behavior in $P6_3mc$ $ScB_6$ correlates with its high coordination structural units. Meanwhile, the strain induces the elongation of B1-B2 and B3-B4 bonds under the tensile deformation along the [110] direction (Fig. S11(c) in the Supplemental Material [65]), which indicates that B1-B2 and B3-B4 bonds are the major load-bearing bonds. The slightly large drop in stress occurs at a tensile strain of 0.19, which is associated with the apparent increase up to 2.94 Å of B1-B2 and B3-B4 distances (Figs. 5(i) and S11(c) in the Supplemental Material [65]). This distance is appreciably >1.89 Å of $P6_3mc$ $ScB_6$ at equilibrium [Fig. 5(h)]. The stress responses under shear strains in the (110) easy cleavage plane of $P6_3mc$ $ScB_6$ are next assessed [Fig. 5(d)]. Interestingly, the isotropic shear stress responses along (110)[001], (110)[$\bar{1}$11], and (110)[$\bar{1}$10] directions are observed in a small range of strains and show progressive enhancement. Upon further shear deformations, the calculated peak at a strain of 0.27 along the (110)[$\bar{1}$11] shear direction is 41.3 GPa, which is even higher than the Vickers hardness of $P6_3mc$ $ScB_6$. The weakest shear stress (i.e., ideal shear strength) of 27.9 GPa is present in the (110)[001] direction at a strain of 0.19 and comparable with 28.2 GPa in the (110)[$\bar{1}$10] direction. Meanwhile, the phonon calculations for two configurations of $P6_3mc$ $ScB_6$ at $\varepsilon = 0.19$ in the (110)[001] and (110)[$\bar{1}$10] shear directions are performed. As demonstrated in Fig. S12 in the Supplemental Material [65], they remain dynamically stable due to the absence of imaginary phonon frequency. Additionally, the shear stress responses of $P6_3mc$ $ScB_6$ under (001)[010], (001) [100], and (001)[110] directions are also examined (Fig. S13 in the Supplemental Material [65]), whose stress peak values are all 27.9 GPa (Table S9 in the Supplemental Material [65]). This further confirms that $P6_3mc$ $ScB_6$ has the weakest shear stress in the (110)[001] direction as well as the (001)[010], (001) [100], and (001)[110] directions. Therefore, the ideal shear strength of $P6_3mc$ $ScB_6$ is higher than its ideal tensile strength (25.3 GPa). Over the peak value, the shear stress in the (110)[001] direction exhibits a slow decrease in comparison with the other two shear slip directions, which is in sharp contrast with that of *Pnma* $ScB_3$. With increasing strain, the steep drop in shear stress in the direction of (110)[001] occurs at $\epsilon = 0.28$, which is identical to that along the (110)[$\bar{1}$11] direction. The abrupt reduction in stress can be elucidated by the B1-B10, B3-B4, B5-B6, B5-B7, B8-B9, and B11-B11 bond breaking, as revealed by the significant elongation of their bond lengths (Figs. 5(j) and

S11(d) in the Supplemental Material [65]). Further analysis demonstrates that there is no B-B bond breakage parallel to the (110) plane under shear deformation along the (110)[001] direction [Fig. 5(j)]. By contrast, two B-B bonds (B3-B4 and B9-B17 bonds) parallel to the (001) plane have broken under shear deformation along the (001)[010] direction (Fig. S13(c) in the Supplemental Material [65]). Overall, the superior mechanical properties of $P6_3mc$ $ScB_6$ and *Pnma* $ScB_3$ are mainly ascribed to the strong boron frameworks with the special atom arrangement patterns.

## IV. CONCLUSIONS

In the quest for potential superhard materials, we achieve a systematic study for Sc-B compounds at ambient and high pressures via advanced structure search and DFT calculations. Intriguingly, we report several unforeseen stable phases including ScB, $ScB_3$, $ScB_4$, $ScB_5$, and a more boron-rich metastable $ScB_6$ phase. Here, *Pnma* $ScB_3$ has an open boron framework, whereas $ScB_6$ possesses interconnecting boron trigons. Furthermore, *Pnma* $ScB_3$ and $P6_3mc$ $ScB_6$ exhibit good dynamic and thermal stability at ambient pressure. Notably, the high Vickers hardness values of 38.3 and 39.8 GPa are obtained in *Pnma* $ScB_3$ and $P6_3mc$ $ScB_6$, respectively, illustrating that they are promising superhard materials. Further ideal strength investigation clearly reveals the deformation mechanism of *Pnma* $ScB_3$ and $P6_3mc$ $ScB_6$, which is primarily contributed by the strong covalent bonds between boron atoms. Moreover, an orthorhombic boron allotrope $o$-$B_{12}$ with potential hardness and superconductivity is gained from *Pnma* $ScB_3$ after the removal of Sc atoms. The insights gained from this paper are of assistance to deepen the understanding of scandium borides and enhance the enrichment of the family of superhard TMBs.

## ACKNOWLEDGMENTS

The authors acknowledge the funding support from the Natural Science Foundation of China under Grants No. 11704062 and No. 12074138, the "111" Project (Grant No. B13013), the Fundamental Research Funds for the Central Universities (Grant No. 2412017QD006), and the Fund from Jilin Province (Grant No. JJKH20221152KJ). The work was carried out at National Supercomputer Center in Tianjin, and the calculations were performed on TianHe-1 (A).

[1] B. Albert and H. Hillebrecht, Boron: Elementary challenge for experimenters and theoreticians, Angew. Chemie Int. Ed. **48**, 8640 (2009).

[2] G. Akopov, M. T. Yeung, and R. B. Kaner, Rediscovering the crystal chemistry of borides, Adv. Mater. **29**, 1604506 (2017).

[3] X.-L. He, X. Shao, T. Chen, Y.-K. Tai, X.-J. Weng, Q. Chen, X. Dong, G. Gao, J. Sun, X.-F. Zhou, Y. Tian, and H.-T. Wang, Predicting three-dimensional icosahedron-based boron $B_{60}$, Phys. Rev. B **99**, 184111 (2019).

[4] Q. Yang, J. Lv, Q. Tong, X. Du, Y. Wang, S. Zhang, G. Yang, A. Bergara, and Y. Ma, Hard and superconducting cubic boron phase via swarm-intelligence structural prediction driven by a machine-learning potential, Phys. Rev. B **103**, 024505 (2021).

[5] K. P. Hilleke, T. Ogitsu, S. Zhang, and E. Zurek, Structural motifs and bonding in two families of boron structures predicted at megabar pressures, Phys. Rev. Materials **5**, 053605 (2021).

[6] A. R. Oganov, J. Chen, C. Gatti, Y. Ma, Y. Ma, C. W. Glass, Z. Liu, T. Yu, O. O. Kurakevych, and V. L. Solozhenko, Ionic high-pressure form of elemental boron, Nature (London) **457**, 863 (2009).

[7] E. Y. Zarechnaya, L. Dubrovinsky, N. Dubrovinskaia, Y. Filinchuk, D. Chernyshov, V. Dmitriev, N. Miyajima, A. El Goresy, H. F. Braun, S. Van Smaalen *et al.*, Superhard Semiconducting Optically Transparent High Pressure Phase of Boron, Phys. Rev. Lett. **102**, 185501 (2009).

[8] S. H. Zhang, X. Zheng, Q. Q. Jin, S. J. Zheng, D. Legut, X. H. Yu, H. Y. Gou, Z. H. Fu, Y. Q. Guo, B. M. Yan, C. Peng, C. Q. Jin, T. C. Germann, and R. F. Zhang, Unprecedented plastic flow channel in $\gamma$-$B_{28}$ through ultrasoft bonds: A challenge to superhardness, Phys. Rev. Materials **2**, 123602 (2018).

[9] S. Zhang, X. Du, J. Lin, A. Bergara, X. Chen, X. Liu, X. Zhang, and G. Yang, Superconducting boron allotropes, Phys. Rev. B **101**, 174507 (2020).

[10] Y. Liang, M. Xu, Z. Qu, S. Lin, J. Hao, and Y. Li, Cage boron allotrope with high superconductivity at ambient pressure, J. Mater. Chem. C **9**, 8258 (2021).

[11] A. G. Van Der Geest and A. N. Kolmogorov, Stability of 41 metal-boron systems at 0 GPa and 30 GPa from first principles, Calphad **46**, 184 (2014).

[12] B. Albert and K. Hofmann, Metal borides: Versatile structures and properties, in *Handbook of Solid State Chemistry*, edited by R. Dronskowski, S. Kikkawa, and A. Stein (Wiley-VCH Verlag, Weinheim, 2017), Chap. 10, pp. 435–454.

[13] Q. Gu, G. Krauss, and W. Steurer, Transition metal borides: Superhard versus ultra-incompressible, Adv. Mater. **20**, 3620 (2008).

[14] G. Akopov, L. E. Pangilinan, R. Mohammadi, and R. B. Kaner, Perspective: Superhard metal borides: A look forward, APL Mater. **6**, 70901 (2018).

[15] M. T. Yeung, R. Mohammadi, and R. B. Kaner, Ultraincompressible, superhard materials, Annu. Rev. Mater. Res. **46**, 465 (2016).

[16] H.-Y. Chung, M. B. Weinberger, J. B. Levine, A. Kavner, J.-M. Yang, S. H. Tolbert, and R. B. Kaner, Synthesis of ultra-incompressible superhard rhenium diboride at ambient pressure, Science **316**, 436 (2007).

[17] J. V. Rau and A. Latini, New hard and superhard materials: $RhB_{1.1}$ and $IrB_{1.35}$, Chem. Mater. **21**, 1407 (2009).

[18] H. Niu, J. Wang, X.-Q. Chen, D. Li, Y. Li, P. Lazar, R. Podloucky, and A. N. Kolmogorov, Structure, bonding, and possible superhardness of $CrB_4$, Phys. Rev. B **85**, 144116 (2012).

[19] B. Petermüller, C. Neun, K. Wurst, L. Bayarjargal, D. Zimmer, W. Morgenroth, M. Avalos-Borja, I. G. Becerril-Juarez, M. J. Mühlbauer, B. Winkler, and H. Huppertz, High-pressure synthesis of $\beta$-$Ir_4B_5$ and determination of the compressibility of various iridium borides, Inorg. Chem. **57**, 10341 (2018).

[20] S. Wei, D. Li, Y. Lv, Z. Liu, C. Xu, F. Tian, D. Duan, B. Liu, and T. Cui, Ground state structures of tantalum tetraboride and triboride: An *ab initio* study, Phys. Chem. Chem. Phys. **18**, 18074 (2016).

[21] X. Li and F. Peng, Predicted superhard phases of Zr-B compounds under pressure, Phys. Chem. Chem. Phys. **21**, 15609 (2019).

[22] Y. Pan, X. Wang, S. Li, Y. Li, and M. Wen, DFT prediction of a novel molybdenum tetraboride superhard material, RSC Adv. **8**, 18008 (2018).

[23] Q. Li, D. Zhou, W. Zheng, Y. Ma, and C. Chen, Global Structural Optimization of Tungsten Borides, Phys. Rev. Lett. **110**, 136403 (2013).

[24] L. Yan-Ling, Z. Guo-Hua, and Z. Zhi, All-electron study of ultra-incompressible superhard material $ReB_2$: Structural and electronic properties, Chinese Phys. B **18**, 4437 (2009).

[25] Y. X. Wang, Y. Y. Liu, Z. X. Yan, W. Liu, G. L. Zhou, and K. Z. Xiong, Crystal structures and mechanical properties of osmium diboride at high pressure, Sci. Rep. **11**, 5754 (2021).

[26] R. Mohammadi, A. T. Lech, M. Xie, B. E. Weaver, M. T. Yeung, S. H. Tolbert, and R. B. Kaner, Tungsten tetraboride, an inexpensive superhard material, Proc. Natl. Acad. Sci. USA **108**, 10958 (2011).

[27] A. G. Kvashnin, H. A. Zakaryan, C. Zhao, Y. Duan, Y. A. Kvashnina, C. Xie, H. Dong, and A. R. Oganov, New tungsten borides, their stability and outstanding mechanical properties, J. Phys. Chem. Lett. **9**, 3470 (2018).

[28] L. Wu, B. Wan, Y. Zhao, Y. Zhang, H. Liu, Y. Wang, J. Zhang, and H. Gou, Unraveling stable vanadium tetraboride and triboride by first-principles computations, J. Phys. Chem. C **119**, 21649 (2015).

[29] A. Knappschneider, C. Litterscheid, D. Dzivenko, J. A. Kurzman, R. Seshadri, N. Wagner, J. Beck, R. Riedel, and B. Albert, Possible superhardness of $CrB_4$, Inorg. Chem. **52**, 540 (2013).

[30] H. Gou, N. Dubrovinskaia, E. Bykova, A. A. Tsirlin, D. Kasinathan, W. Schnelle, A. Richter, M. Merlini, M. Hanfland, A. M. Abakumov, D. Batuk, G. Van Tendeloo, Y. Nakajima, A. N. Kolmogorov, and L. Dubrovinsky, Discovery of a Superhard Iron Tetraboride Superconductor, Phys. Rev. Lett. **111**, 157002 (2013).

[31] M. Zhang, M. Lu, Y. Du, L. Gao, C. Lu, and H. Liu, Hardness of $FeB_4$: Density functional theory investigation, J. Chem. Phys. **140**, 174505 (2014).

[32] J. Wang, X. Song, X. Shao, B. Gao, Q. Li, and Y. Ma, High-pressure evolution of unexpected chemical bonding and promising superconducting properties of $YB_6$, J. Phys. Chem. C **122**, 27820 (2018).

[33] L.-P. Ding, Y. H. Tiandong, P. Shao, Y. Tang, Z.-L. Zhao, and H. Lu, Crystal structures, phase stabilities, electronic properties, and hardness of yttrium borides: New insight from first-principles calculations, J. Phys. Chem. Lett. **12**, 5423 (2021).

[34] Y. Liang, M. Xu, S. Lin, X. Yuan, Z. Qu, J. Hao, and Y. Li, Pressure-induced boron clathrate with ambient-pressure superconductivity, J. Mater. Chem. C **9**, 13782 (2021).

[35] L. Ma, X. Yang, G. Liu, H. Liu, G. Yang, H. Wang, J. Cai, M. Zhou, and H. Wang, Design and synthesis of clathrate $LaB_8$ with superconductivity, Phys. Rev. B **104**, 174112 (2021).

[36] T. Ma, H. Li, X. Zheng, S. Wang, X. Wang, H. Zhao, S. Han, J. Liu, R. Zhang, P. Zhu, Y. Long, J. Cheng, Y. Ma, Y. Zhao, C. Jin, and X. Yu, Ultrastrong boron frameworks in $ZrB_{12}$: a highway for electron conducting, Adv. Mater. **29**, 1604003 (2017).

[37] G. Levchenko, A. Lyashchenko, V. Baumer, A. Evdokimova, V. Filippov, Y. Paderno, and N. Shitsevalova, Preparation and some properties of $ScB_2$ single crystals, J. Solid State Chem. **179**, 2949 (2006).

[38] M. Przybylska, A. H. Reddoch, and G. J. Ritter, The preparation and structure of lutetium diboride, scandium dodecaboride and lutetium antimonide, J. Am. Chem. Soc. **85**, 407 (1963).

[39] A. Pediaditakis, S. Haseloff, and H. Hillebrecht, Single crystal investigations on $ScB_{15}$ and $Sc_2Cu_{1-x}B_{45}$—two new representatives of boron-rich borides related to tetragonal boron II ($t$-B192), Solid State Sci. **13**, 1465 (2011).

[40] T. Tanaka, S. Okada, and V. N. Gurin, A new scandium boride: $ScB_{19}$, J. Alloys Compd. **267**, 211 (1998).

[41] I. R. Shein and A. L. Ivanovskii, Elastic properties of mono- and polycrystalline hexagonal $AlB_2$-like diborides of $s$, $p$ and $d$ metals from first-principles calculations, J. Phys. Condens. Matter **20**, 415218 (2008).

[42] T. Bai, G. Zhang, Y. Zhao, L. Chen, B. Mu, Y. Han, and Q. Wei, First-principles prediction of crystal structure and physical properties of $ScB_3$, Mol. Phys. **118**, e1603411 (2020).

[43] V. I. Matkovich, J. Economy, R. F. Giese, and R. Barrett, The structure of metallic dodecarborides, Acta Crystallogr. **19**, 1056 (1965).

[44] J.-O. Carlsson and T. Lundstroem, The solution hardening of $\beta$-rhombohedral boron, J. Less Common Met. **22**, 317 (1970).

[45] M. Zhang, H. Wang, H. Wang, X. Zhang, T. Iitaka, and Y. Ma, First-principles prediction on the high-pressure structures of transition metal diborides ($TMB_2$, $TM$ = Sc, Ti, Y, Zr), Inorg. Chem. **49**, 6859 (2010).

[46] B.-H. Chu and Y. Zhao, Prediction of scandium tetraboride from first-principles calculations: Crystal structures, phase stability, mechanical properties, and hardness, Chinese Phys. B **30**, 76107 (2021).

[47] Y. Wang, J. Lv, L. Zhu, and Y. Ma, Crystal structure prediction via particle-swarm optimization, Phys. Rev. B **82**, 094116 (2010).

[48] Y. Wang, J. Lv, L. Zhu, and Y. Ma, CALYPSO: A method for crystal structure prediction, Comput. Phys. Commun. **183**, 2063 (2012).

[49] S. Zhang, L. Zhu, H. Liu, and G. Yang, Structure and electronic properties of $Fe_2SH_3$ compound under high pressure, Inorg. Chem. **55**, 11434 (2016).

[50] Y. Li, J. Hao, H. Liu, Y. Li, and Y. Ma, The metallization and superconductivity of dense hydrogen sulfide, J. Chem. Phys. **140**, 174712 (2014).

[51] L. Zhang, Y. Wang, J. Lv, and Y. Ma, Materials discovery at high pressures, Nat. Rev. Mater. **2**, 17005 (2017).

[52] J. Lv, Y. Wang, L. Zhu, and Y. Ma, Predicted Novel High-Pressure Phases of Lithium, Phys. Rev. Lett. **106**, 015503 (2011).

[53] L. Zhu, H. Wang, Y. Wang, J. Lv, Y. Ma, Q. Cui, Y. Ma, and G. Zou, Substitutional Alloy of Bi and Te at High Pressure, Phys. Rev. Lett. **106**, 145501 (2011).

[54] H. Wang, S. T. John, K. Tanaka, T. Iitaka, and Y. Ma, Superconductive sodalite-like clathrate calcium hydride at high pressures, Proc. Natl. Acad. Sci. USA **109**, 6463 (2012).

[55] Q. Yang, K. Zhao, H. Liu, and S. Zhang, Superconductive sodium carbides with pentagon carbon at high pressures, J. Phys. Chem. Lett. **12**, 5850 (2021).

[56] S. Zhang, Q. Yang, X. Zhang, K. Zhao, H. Yu, L. Zhu, and H. Liu, Crystal structures and superconductivity of lithium and fluorine implanted gold hydrides under high pressures, Phys. Chem. Chem. Phys. **23**, 21544 (2021).

[57] J. Zhang, H. Liu, Y. Ma, and C. Chen, Direct H-He chemical association in superionic $FeO_2H_2He$ at deep-earth conditions, Natl. Sci. Rev. nwab168 (2021), doi: 10.1093/nsr/nwab168.

[58] P. Hohenberg and W. Kohn, Density functional theory (DFT), Phys. Rev. **136**, B864 (1964).

[59] W. Kohn and L. J. Sham, Self-consistent equations including exchange and correlation effects, Phys. Rev. **140**, A1133 (1965).

[60] G. Kresse and J. Furthmüller, Efficient iterative schemes for *ab initio* total-energy calculations using a plane-wave basis set, Phys. Rev. B **54**, 11169 (1996).

[61] J. P. Perdew, J. A. Chevary, S. H. Vosko, K. A. Jackson, M. R. Pederson, D. J. Singh, and C. Fiolhais, Erratum: Atoms, molecules, solids, and surfaces: Applications of the generalized gradient approximation for exchange and correlation, Phys. Rev. B **48**, 4978(E) (1993).

[62] J. P. Perdew, K. Burke, and M. Ernzerhof, Generalized Gradient Approximation Made Simple, Phys. Rev. Lett. **77**, 3865 (1996).

[63] P. E. Blöchl, Projector augmented-wave method, Phys. Rev. B **50**, 17953 (1994).

[64] P. Blaha, K. Schwarz, P. Sorantin, and S. B. Trickey, Full-potential, linearized augmented plane wave programs for crystalline systems, Comput. Phys. Commun. **59**, 399 (1990).

[65] See Supplemental Material at http://link.aps.org/supplemental/10.1103/PhysRevB.105.094104 for computational details; phonon dispersion curves, electronic band structures, PDOS, and ELF of predicted Sc-B phases; COHP of adjacent Sc-B and B-B pairs in *Pnma* $ScB_3$ and $P6_3mc$ $ScB_6$ at 1 atm; and mechanical properties for *Pnma* $ScB_3$, $P6_3mc$ $ScB_6$, and *Pnma* $B_{12}$ at 1 atm.

[66] H. J. Monkhorst and J. D. Pack, Special points for Brillouin-zone integrations, Phys. Rev. B **13**, 5188 (1976).

[67] A. Togo, F. Oba, and I. Tanaka, First-principles calculations of the ferroelastic transition between rutile-type and $CaCl_2$ type $SiO_2$ at high pressures, Phys. Rev. B **78**, 134106 (2008).

[68] K. Parlinski, Z. Q. Li, and Y. Kawazoe, First-Principles Determination of the Soft Mode in Cubic Mathrm $ZrO_2$, Phys. Rev. Lett. **78**, 4063 (1997).

[69] G. J. Martyna, M. L. Klein, and M. Tuckerman, Nosé-Hoover chains: The canonical ensemble via continuous dynamics, J. Chem. Phys. **97**, 2635 (1992).

[70] R. Hill, The elastic behaviour of a crystalline aggregate, Proc. Phys. Soc. A **65**, 349 (1952).

[71] Y. Le Page and P. Saxe, Symmetry-general least-squares extraction of elastic data for strained materials from *ab initio* calculations of stress, Phys. Rev. B **65**, 104104 (2002).

[72] F. H. Spedding, J. J. Hanak, and A. H. Daane, High temperature allotropy and thermal expansion of the rare-earth metals, J. Less Common Met. **3**, 110 (1961).

[73] S.-C. Zhu, X.-Z. Yan, S. Fredericks, Y.-L. Li, and Q. Zhu, First-principles investigation of Sc-III/IV under high pressure, Phys. Rev. B **98**, 214116 (2018).

[74] Y. Akahama, H. Fujihisa, and H. Kawamura, New Helical Chain Structure for Scandium at 240 GPa, Phys. Rev. Lett. **94**, 195503 (2005).

[75] J. Feng, R. G. Hennig, N. W. Ashcroft, and R. Hoffmann, Emergent reduction of electronic state dimensionality in dense ordered Li-Be alloys, Nature (London) **451**, 445 (2008).

[76] Y. Wu, P. Lazic, G. Hautier, K. Persson, and G. Ceder, First principles high throughput screening of oxynitrides for water-splitting photocatalysts, Energy Environ. Sci. **6**, 157 (2013).

[77] Y. Hinuma, T. Hatakeyama, Y. Kumagai, L. A. Burton, H. Sato, Y. Muraba, S. Iimura, H. Hiramatsu, I. Tanaka, and H. Hosono, Discovery of earth-abundant nitride semiconductors by computational screening and high-pressure synthesis, Nat. Commun. **7**, 11962 (2016).

[78] A. Hermann, A. McSorley, N. W. Ashcroft, and R. Hoffmann, From Wade-Mingos to Zintl-Klemm at 100 GPa: Binary compounds of boron and lithium, J. Am. Chem. Soc. **134**, 18606 (2012).

[79] F. Mouhat and F.-X. Coudert, Necessary and sufficient elastic stability conditions in various crystal systems, Phys. Rev. B **90**, 224104 (2014).

[80] D. Y. Kim, S. Stefanoski, O. O. Kurakevych, and T. A. Strobel, Synthesis of an open-framework allotrope of silicon, Nat. Mater. **14**, 169 (2015).

[81] H.-J. Sung, W. H. Han, I.-H. Lee, and K. J. Chang, Superconducting Open-Framework Allotrope of Silicon at Ambient Pressure, Phys. Rev. Lett. **120**, 157001 (2018).

[82] R. Dronskowski and P. E. Bloechl, Crystal orbital Hamilton populations (COHP): Energy-resolved visualization of chemical bonding in solids based on density-functional calculations, J. Phys. Chem. **97**, 8617 (1993).

[83] S. Maintz, V. L. Deringer, A. L. Tchougréeff, and R. Dronskowski, LOBSTER: A tool to extract chemical bonding from plane-wave based DFT, J. Comput. Chem. **37**, 1030 (2016).

[84] P. B. Allen and R. C. Dynes, Transition temperature of strong-coupled superconductors reanalyzed, Phys. Rev. B **12**, 905 (1975).

[85] W. L. McMillan, Transition temperature of strong-coupled superconductors, Phys. Rev. **167**, 331 (1968).

[86] J. Bardeen, L. N. Cooper, and J. R. Schrieffer, Theory of superconductivity, Phys. Rev. **108**, 1175 (1957).

[87] X.-Q. Chen, H. Niu, D. Li, and Y. Li, Modeling hardness of polycrystalline materials and bulk metallic glasses, Intermetallics **19**, 1275 (2011).

[88] S. Vepřek, The search for novel, superhard materials, J. Vac. Sci. Technol. A **17**, 2401 (1999).

[89] V. L. Solozhenko and E. Gregoryanz, Synthesis of superhard materials, Mater. Today **8**, 44 (2005).

[90] J. Haines, J. M. Leger, and G. Bocquillon, Synthesis and design of superhard materials, Annu. Rev. Mater. Res. **31**, 1 (2001).

[91] Z. Zhao, B. Xu, and Y. Tian, Recent advances in superhard materials, Annu. Rev. Mater. Res. **46**, 383 (2016).

[92] H. Niu, S. Niu, and A. R. Oganov, Simple and accurate model of fracture toughness of solids, J. Appl. Phys. **125**, 65105 (2019).

[93] R. H. Telling, C. J. Pickard, M. C. Payne, and J. E. Field, Theoretical Strength and Cleavage of Diamond, Phys. Rev. Lett. **84**, 5160 (2000).

[94] H. Chacham and L. Kleinman, Instabilities in Diamond under High Shear Stress, Phys. Rev. Lett. **85**, 4904 (2000).

[95] C. Lu, Q. Li, Y. Ma, and C. Chen, Extraordinary Indentation Strain Stiffening Produces Superhard Tungsten Nitrides, Phys. Rev. Lett. **119**, 115503 (2017).

[96] S.-H. Jhi, S. G. Louie, M. L. Cohen, and J. W. Morris, Mechanical Instability and Ideal Shear Strength of Transition Metal Carbides and Nitrides, Phys. Rev. Lett. **87**, 075503 (2001).

[97] S. Ogata, J. Li, N. Hirosaki, Y. Shibutani, and S. Yip, Ideal shear strain of metals and ceramics, Phys. Rev. B **70**, 104104 (2004).

[98] X. Blase, P. Gillet, A. San Miguel, and P. Mélinon, Exceptional Ideal Strength of Carbon Clathrates, Phys. Rev. Lett. **92**, 215505 (2004).

[99] Y. Zhang, H. Sun, and C. Chen, Superhard Cubic $BC_2N$ Compared to Diamond, Phys. Rev. Lett. **93**, 195504 (2004).

[100] Y. Zhang, H. Sun, and C. Chen, Atomistic Deformation Modes in Strong Covalent Solids, Phys. Rev. Lett. **94**, 145505 (2005).

[101] Q. Li, D. Zhou, W. Zheng, Y. Ma, and C. Chen, Anomalous Stress Response of Ultrahard $WB_n$ Compounds, Phys. Rev. Lett. **115**, 185502 (2015).

[102] Y. Zhang, H. Sun, and C. Chen, Structural deformation, strength, and instability of cubic BN compared to diamond: A first-principles study, Phys. Rev. B **73**, 144115 (2006).

[103] M. Zhang, H. Liu, Q. Li, B. Gao, Y. Wang, H. Li, C. Chen, and Y. Ma, Superhard $BC_3$ in Cubic Diamond Structure, Phys. Rev. Lett. **114**, 015502 (2015).

[104] W. Lu, H. Zhai, Q. Li, and C. Chen, Pronounced enhancement of superconductivity in ZrN via strain engineering, J. Phys. Chem. Lett. **12**, 1985 (2021).